Nanoscale Advances

ROYAL SOCIETY OF CHEMISTRY

PAPER

View Article Online
View Journal | View Issue

Cite this: *Nanoscale Adv.*, 2025, **7**, 506

Tungsten oxide nanowire clusters anchored on porous carbon fibers as a sulfur redox mediator for lithium–sulfur batteries†

Tongzhen Wang,[a] Xiaofei Zhang,[a] Jie Yang,[a] Jiewu Cui,[a] Jian Yan,[a] Jiaqin Liu *[b] and Yucheng Wu *[a]

Addressing the sluggish redox kinetics of sulfur electrodes and mitigating the shuttle effect of intermediate lithium polysulfides (LiPS) are crucial for the advancement of high-energy lithium–sulfur batteries. Here, we introduce a pioneering flexible self-supporting composite scaffold that incorporates tungsten oxide nanowire clusters anchored on core–shell porous carbon fibers (WO_3/PCF) for sulfur accommodation. The core of PCF serves as a robust electrode supporting scaffold, whereas the porous shell of PCF provides a 3D interconnected conductive network to accommodate sulfur, restrain polysulfide diffusion and buffer electrode expansion. The WO_3 nanowire clusters not only entrap polysulfides but also function as a redox mediator to promote sulfur conversion, thus greatly mitigating the shuttle effect and boosting redox kinetics. The unique core–shell porous structure of PCF and the dual functionality of WO_3 for LiPS capture and conversion contribute to the high capacity, exceptional cycling stability, and superior rate capability of the WO_3/PCF/S cathode. Impressively, at a sulfur loading of 3.0 mg cm^{-2}, it achieves an initial capacity of 1082 mA h·g^{-1} at 1 C with an ultralow decay rate of 0.039% over 1000 cycles. Even under a high sulfur loading of 6.1 mg cm^{-2}, it maintains a reversible capacity of 536 mA h·g^{-1} after 1000 cycles with a decay rate of only 0.043% at 0.5 C.

Received 5th October 2024
Accepted 21st November 2024

DOI: 10.1039/d4na00829d

rsc.li/nanoscale-advances

Introduction

Lithium–sulfur batteries (LSBs) offer a high theoretical specific capacity of 1675 mA h g^{-1} and energy density of 2600 W h kg^{-1}, significantly surpassing lithium-ion batteries (LIBs), driven by their complex sulfur-mediated redox reactions.[1,2] Coupled with abundant sulfur reserves, cost-effectiveness, and environmental benefits, lithium–sulfur batteries are positioned as a leading contender for future sustainable energy solutions.[2,3] Despite these advantages, the complex multiphase conversion chemistry of sulfur still faces several challenges, such as the insulating nature of sulfur and discharge products of Li_2S_2/Li_2S, the notorious shuttle effect of lithium polysulfides (LiPS), slow sulfur redox kinetics, and electrode volume expansion during charging/discharging, leading to low coulombic efficiency, short cycle life, and rapid capacity fading.[4,5]

To address these challenges, significant advancements have been made, such as the development of nanocomposite sulfur cathodes,[6,7] functional separators/interlayers,[8,9] solid-state electrolytes,[10,11] *etc.* Among these, sulfur cathode design remains critical for improving the performance of lithium–sulfur batteries, but it continues to face significant hurdles, particularly in managing severe LiPS shuttling and sluggish redox kinetics of sulfur. Research has primarily focused on strategies that physically confine sulfur species within porous carbon materials and chemically anchor and catalyze the redox reaction of LiPS on polar materials. Various polar materials (such as single atoms,[12,13] metal oxides,[14,15] metal sulfides,[16,17] metal nitrides,[18] metal carbides,[19] metal phosphides,[20] *etc.*) have been incorporated into the carbon matrix to enhance LiPS absorption and act as electrocatalysts to accelerate redox kinetics, thus facilitating a stable LiPS "capture-conversion" process on the electrode surface.

For practical applications, lithium–sulfur batteries require a high sulfur loading on the cathode (>4 mg cm^{-2}) and a high sulfur-to-carbon ratio (>70%).[7,21] However, these requirements are constrained by sluggish charge/mass transfer kinetics within the electrode, which aggravates the challenges of slow sulfur redox kinetics, polysulfide shuttling, and electrode volume expansion. Conventional sulfur cathode materials, typically in powder form, require blending with conductive additives and binders, followed by coating onto a current

[a]*School of Materials Science and Engineering, Hefei University of Technology, Hefei 230009, China. E-mail: ycwu@hfut.edu.cn*

[b]*Institute of Industry and Equipment Technology, Research Center of Advanced Composite Materials Design & Application of Anhui Province, Key Laboratory of Advanced Functional Materials and Devices of Anhui Province, Hefei University of Technology, Hefei, 230009, China. E-mail: jqliu@hfut.edu.cn*

† Electronic supplementary information (ESI) available. See DOI: https://doi.org/10.1039/d4na00829d

collector. This process reduces the specific mass-energy density of batteries since conductive additives, binders, and the current collector do not contribute to capacity. Additionally, the electrochemically inert nature of binders obscures active sites and increases internal resistance, further hindering ion and electron transport.[22,23] Therefore, innovating the design of the sulfur cathode structure by integrating active materials with current collectors and developing unique self-supporting sulfur cathode structures with high sulfur loading and "strong adsorption-rapid conversion" capabilities for LiPS is crucial for advancing the development of lithium–sulfur batteries.

Herein, we introduce a flexible, self-supporting composite scaffold featuring tungsten oxide nanowire clusters anchored on core–shell porous carbon fibers (WO_3/PCF) for sulfur accommodation, which was achieved using a combined strategy of metal-assisted chemical etching followed by hydrothermal-annealing techniques. The core of PCF serves as a robust electrode supporting scaffold, while the porous carbon shell forms a 3D interconnected conductive network to accommodate active sulfur, restrain polysulfide diffusion, and buffer electrode volume expansion. The WO_3 nanowire clusters not only entrap polysulfides but also function as a redox mediator to promote sulfur conversion, thereby significantly mitigating the shuttle effect and improving redox kinetics. Consequently, lithium–sulfur batteries based on the WO_3/PCF/S cathode demonstrate superior electrochemical performance, including high capacity, exceptional cycle stability, superior rate capability, and low self-discharge.

Experimental section

Preparation of WO_3/PCF

Porous carbon fibers (PCF) were synthesized using a metal-assisted chemical etching technique. Initially, carbon fiber cloth was sequentially cleaned ultrasonically in acetone, ethanol, and deionized water. Nickel hydroxide ($Ni(OH)_2$) was then electrochemically deposited onto the carbon fiber surface in a three-electrode system, with the carbon fiber cloth as the working electrode, Ag/AgCl as the reference electrode, and platinum (Pt) as the counter electrode. The electrolyte consisted of 1 mol L^{-1} $Ni(NO_3)_2$ and 0.1 mol L^{-1} $NaNO_3$. The electrodeposition current density and time were 6 mA cm^{-2} and 900 s, respectively. Following deposition, the samples were calcined at 800 °C at a heating rate of 5 °C min^{-1} in a nitrogen atmosphere for 4 hours. Following calcination, the samples were immersed in 3 mol L^{-1} hydrochloric acid at 80 °C for 6 hours and then rinsed with deionized water to yield PCF. The average mass density of PCF was approximately 7.0 mg cm^{-2}.

Subsequently, tungsten oxide (WO_3) nanowire clusters were deposited onto the PCF surface *via* a hydrothermal method. A precursor solution containing 0.5 mol L^{-1} Na_2WO_4 and 0.3 mol L^{-1} $H_2C_2O_4$ was prepared and adjusted to pH = 0.8 using 3 M HCl. Then, 2 g of $(NH_4)_2SO_4$ was dissolved in 30 mL of the precursor solution. The PCF was immersed in this solution and placed in a 50 mL reactor, which was then heated at 180 °C for 12 hours. After the reaction, the sample was washed with deionized water, dried, and annealed at 400 °C with a heating rate of 3 °C min^{-1} under a nitrogen atmosphere for 4 hours to obtain WO_3/PCF. The areal mass density of WO_3/PCF was approximately 10.0 mg cm^{-2}, and its thickness is around 370 μm (Fig. S1†).

Preparation of WO_3/PCF/S

Sulfur was incorporated into the WO_3/PCF host using a melt-diffusion method. The WO_3/PCF host was mixed with excess sulfur powder in a reaction vessel and maintained at 155 °C for 12 hours. The temperature was then raised to 175 °C to remove surplus sulfur from the surface and control the final sulfur loading, producing the flexible self-supporting sulfur cathode of WO_3/PCF/S. Similar procedures were followed for the preparation of WO_3/CF/S and PCF/S cathodes.

Visualized adsorption test

A 5 mM Li_2S_6 solution was first prepared by dissolving Li_2S and sulfur at a 5 : 1 molar ratio in a mixed solvent of 1,3-dioxolane (DOL)/1,2-dimethoxyethane (DME) (1 : 1 in volume) at 60 °C for 12 hours. For the static adsorption test, equal-sized WO_3/PCF, WO_3/CF, and PCF were immersed in 5 mL of the above Li_2S_6 solution. After standing for 8 hours, the adsorption capacity of the samples towards LiPS was evaluated by comparing the decolorization of the Li_2S_6 solution. All procedures were conducted in an argon-filled glove box. The adsorption capacities were subsequently quantified by analyzing the UV-vis absorption spectra of the Li_2S_6 solution post-adsorption.

Materials characterization

The morphologies and microstructures were characterized by field-emission scanning electron microscopy (FESEM, ZEISS Sigma 300) and high-resolution transmission electron microscopy (HRTEM, JEM-2100F). Phase structures were identified by X-ray diffraction (XRD) analysis conducted on a Rigaku D/MAX2500V/PC with Cu-Kα radiation (λ = 0.154056 nm). Elemental composition and chemical states were examined using X-ray photoelectron spectroscopy (XPS, Escalab250Xi) and Raman spectroscopy (Raman, LabRAM HR Evolution, HORIBA Jobin-Yvon) with a 532 nm excitation laser. The specific surface area and pore size distribution were assessed using an automatic gas adsorption analyzer (Autosorb-IQ3, Quantachrome). Areal sulfur loading was determined using a Pyris 1 TGA (PerkinElmer) thermal analyzer from 0 to 600 °C at a heating rate of 5 °C min^{-1}.

Cell assembly and electrochemical measurements

CR2032-type cells were assembled with WO_3/PCF/S, WO_3/CF/S, and PCF/S as the cathodes, lithium metal (approximately 490 μm thick, Fig. S1†) as the anode, a Celgard 2500 polypropylene (PP) membrane as the separator, and an electrolyte of 1 mol L^{-1} LiTFSI with 1 wt% $LiNO_3$ in a 1 : 1 volume ratio of DOL/DME. The electrolyte-to-sulfur (E/S) ratio for Li–S cell assembly was set at 12 μL mg^{-1}. All procedures were performed in a glove box under an argon atmosphere (O_2, H_2O < 0.1 ppm). Cyclic charge/discharge tests were conducted using a Land battery test system

(CT2001A, Wuhan) within a voltage range of 1.7–2.8 V. Cyclic voltammetry (CV) and electrochemical impedance spectroscopy (EIS) measurements were carried out using an electrochemical workstation (Autolab PGSTAT302N). CV was performed at a scan rate of 0.1 mV s^{-1} within a voltage range of 1.7–2.8 V, and EIS was performed in the frequency range from 100 kHz to 10 mHz with an amplitude of 5 mV s^{-1}. For shuttle current evaluation, CR2032-type cells were assembled with 1.0 M LiTFSI in DME/DOL solution as the electrolyte. The cells underwent an initial two cycles at 0.05 C, followed by galvanostatic discharge to 1.7 V, charging to 2.38 V, and holding at this potential until the current stabilized, indicating the shuttle current. Symmetrical cells were assembled with WO_3/PCF, WO_3/CF, and PCF as electrodes, a Celgard 2500 as the separator, and 0.2 mol·L^{-1} Li_2S_6 solution as the electrolyte. CV of symmetrical cells was conducted at a scan rate of 0.3 mV s^{-1} from −1 to 1 V.

Calculation methods

Density functional theory (DFT) calculations were performed using the VASP 5.4 package.[24,25] The electronic exchange–correlation interactions were described using the Perdew–Burke–Ernzerhof (PBE) functional under the Generalized Gradient Approximation (GGA).[26] A 3 × 3 × 1 supercell was utilized to simulate the WO_3 (002) surface. The Brillouin zone was sampled using a 2 × 2 × 1 Monkhorst–Pack grid for structural optimization and energy calculations.[27] Convergence thresholds were set at 1×10^{-5} eV for energy and 0.01 eV $Å^{-1}$ for atomic forces, with a plane-wave cutoff energy of 520 eV. A vacuum layer of 15 Å along the *Z*-axis direction was employed to prevent interactions between layers.

The adsorption energy of S_8 and Li_2S_n ($n = 1, 2, 4, 6, 8$) on the WO_3 (002) surface was calculated as

$$E_{ad} = E_{S_8/Li_2S_n@WO_3} - E_{WO_3} - E_{S_8/Li_2S_n}$$

where $E_{S_8/Li_2S_n@WO_3}$ represents the total energy of S_8/Li_2S_n adsorbed on the WO_3 (002) surface, E_{WO_3} is the energy of the WO_3 (002) surface, and E_{S_8/Li_2S_n} is the energy of the isolated S_8 or Li_2S_n molecules.[28]

Results and discussion

A metal-assisted chemical etching strategy was employed to controllably etch the carbon fiber (CF) skeleton, producing hierarchical porous carbon fiber (PCF) with a distinctive core–shell structure, as shown in Fig. 1a. In contrast to the initial CF (Fig. S2†), the surface of PCF was etched into a hierarchical porous carbon layer approximately 2 μm thick, while the inner core of PCF maintained a solid fiber structure, forming a core–shell structure (Fig. 2a). BET analysis reveals a high specific surface area of 323.3 m^2 g^{-1} and a micro-mesoporous structure for the PCF shell (Fig. S3†). The specific surface area of the PCF shell was calculated by excluding the mass of the PCF core. The PCF core functions as a robust electrode supporting scaffold, while the porous PCF shell provides a 3D interconnected conductive network to accommodate active sulfur, buffer electrode volume expansion, and physically immobilize polysulfide, thus preventing sulfur loss within the PCF. Upon loading WO_3 onto the PCF, the surface of the PCF was fully covered by "tower-like" WO_3 nanowire clusters (Fig. 2b and d). These nanowires were approximately 1 μm in length and 15–25 nm in diameter. The clusters contain numerous voids, both within and between them, offering ample space for sulfur accommodation and enhancing electrolyte infiltration. EDS mapping of WO_3/PCF (Fig. 2c) shows a uniform distribution of W, O and C elements, indicating that WO_3 nanowires were evenly anchored on the PCF surface. A single WO_3 nanowire (Fig. S4†) shows a tapered structure with a wide base and a sharp tip. The high-resolution TEM image (Fig. 2e and f) displays distinct lattice fringes with an interplanar spacing of 0.38 nm, corresponding to the (002) plane of WO_3. The selected area electron diffraction (SAED) patterns (Fig. 2g) align well with the (002), (022) and (322) planes of WO_3. Upon sulfur loading, active sulfur infiltrates the porous shell layer of PCF and uniformly encapsulates the WO_3 nanowire surfaces (Fig. S5a and b†). EDS mapping confirms the even distribution of sulfur across WO_3/PCF, without agglomeration observed on the surface or within the internal voids of the WO_3 nanowire clusters (Fig. S5c†).

The phase structures of PCF, WO_3/PCF, and WO_3/PCF/S were characterized using X-ray diffraction (XRD), as illustrated in Fig. 2h. The XRD pattern of PCF reveals a prominent peak of graphitized carbon at $2\theta \approx 26°$. For WO_3/PCF, additional diffraction peaks at $2\theta \approx 23.1°$, 23.6°, 24.4°, 26.6°, 28.9°, 33.3°, 34.2°, 41.4°, 50.3°, and 55.8° align well with the characteristic peaks of WO_3 (PDF No. 071-2141), confirming successful deposition of WO_3 nanowire clusters on the PCF surface. Following sulfur loading onto WO_3/PCF, new weak diffraction peaks emerged at $2\theta \approx 20.8°$ and 27.7° with other peaks overlapping WO_3 peaks, consistent with elemental sulfur (PDF No. 53-1109), indicating effective sulfur incorporation into the WO_3/PCF scaffold. The weak sulfur peaks suggest sulfur infiltration into the porous PCF shell and encapsulation on the WO_3 nanowire surfaces, without sulfur agglomeration on the surface or within the internal voids of the WO_3 nanowire clusters. The Raman spectra of PCF, WO_3/PCF, and WO_3/PCF/S (Fig. 2i) display characteristic peaks for D and G bands of carbon at 1346 and 1597 cm^{-1}. The I_D/I_G ratio of WO_3/PCF (1.07) and WO_3/PCF/S was slightly lower than that of PCF (1.10), which ensures good conductivity that favors sulfur conversion.[29] Notably, the Raman spectra of WO_3/PCF and WO_3/PCF/S display WO_3 peaks at 694 cm^{-1}, 803 cm^{-1}, 941 cm^{-1}, 252 cm^{-1}, and 322 cm^{-1},[30,31] along with sulfur peaks at 152 cm^{-1}, 221 cm^{-1} and 475 cm^{-1} for WO_3/PCF/S after sulfur loading.[32] The elemental composition and chemical states of WO_3/PCF were further investigated using X-ray photoelectron spectroscopy (XPS). The XPS survey spectrum (Fig. S6†) shows peaks at binding energies of 285.4, 531.5 and 37.2 eV, corresponding to the characteristic peaks of C 1s, O 1s and W 4f, respectively, indicating the presence of W, C and O elements in WO_3/PCF. The C 1s spectrum (Fig. 2j) includes three fitted peaks corresponding to C–C (284.8 eV), C–O/C–O–C (286.3 eV), and O=C–O (288.9 eV).[33,34] The W 4f spectrum (Fig. 2k) features peaks at binding energies of 35.8 and 38.0 eV, corresponding to the W $4f_{7/2}$ and W $4f_{5/2}$ of W^{6+} in WO_3, respectively.[35,36] In the O 1s spectrum (Fig. 2l), the peak at

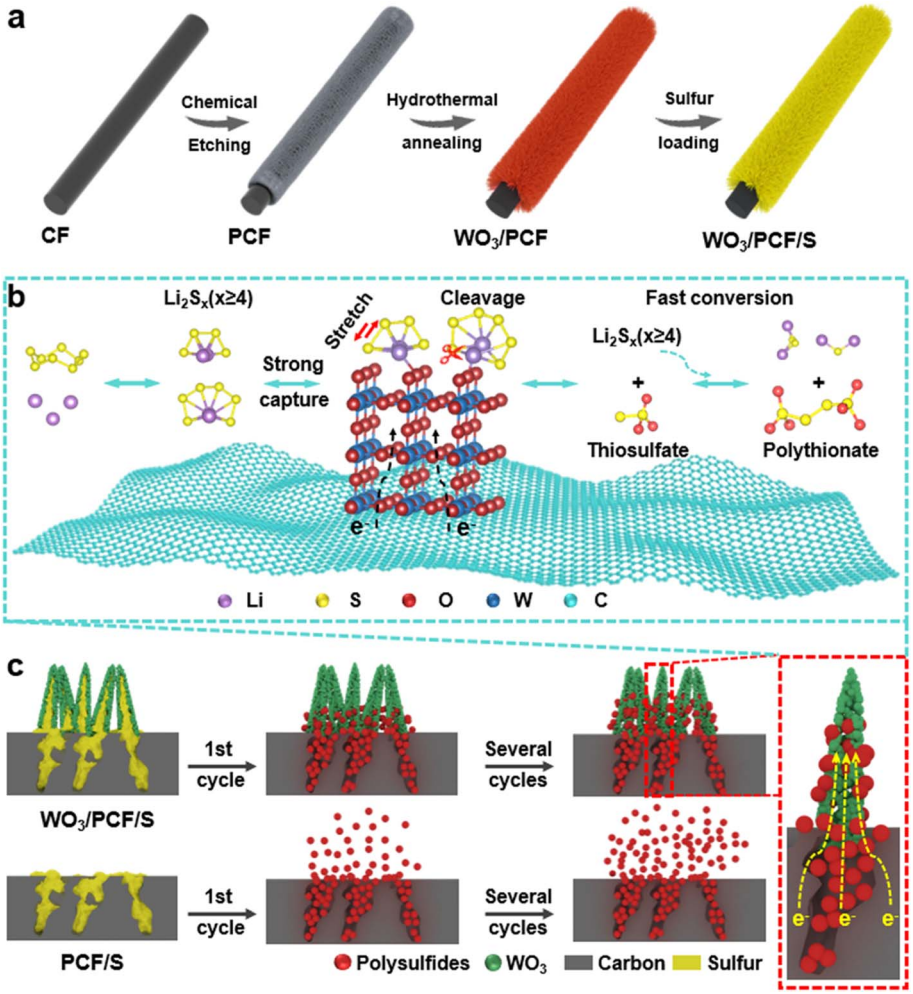

Fig. 1 (a) Schematic illustration of the WO_3/PCF/S synthesis process, (b) LiPS conversion catalyzed on the WO_3/PCF surface, and (c) dual-blocking effects associated with "physical constraint and adsorption-catalysis" towards polysulfides within the WO_3/PCF/S electrode.

a binding energy of 530.7 eV corresponds to the W–O bond, while peaks at 532.0 and 533.1 eV are attributed to hydroxyl or carbonate contaminants on the WO_3/PCF surface.[36] TGA analysis (Fig. S7†) reveals sulfur contents of approximately 23.8 and 30.4 wt% for WO_3/PCF/S and PCF/S cathodes, respectively, at an areal sulfur loading of 3.0 mg cm^{-2}.

The adsorption capability of host materials towards LiPS was indicative of their ability to mitigate the shuttle effect. To assess the LiPS absorbing capacity, a visual adsorption test was conducted by immersing WO_3/PCF, WO_3/CF, and PCF in a Li_2S_6 solution and monitoring the decolorization of the Li_2S_6 solution over time (Fig. 3a). It was evident that after adsorption, the Li_2S_6 solution with WO_3/PCF changed from deep yellow to almost clear. The degree of decolorization follows the order: WO_3/PCF > WO_3/CF > PCF. This observation was confirmed by the disappearance of the characteristic UV-vis peak for Li_2S_6 at 411 nm,[37] demonstrating that WO_3 has a strong adsorption capacity towards LiPS. The interaction mechanism between WO_3 and LiPS was further explored by XPS analysis. After adsorption, the S 2p peak at 169.3 eV emerged in the survey spectrum of WO_3/PCF-Li_2S_6 (Fig. S6†). The high-resolution S 2p spectrum (Fig. 3b) can be deconvoluted into four pairs of doublets: two pairs correspond to the terminal sulfur (S_T^{-1}) and bridging sulfur (S_B^0) of adsorbed Li_2S_6, while the other two pairs were attributed to thiosulfate and polythionate complexes,[38,39] generated by the redox reaction of Li_2S_6 with WO_3 and further reaction of thiosulfate with Li_2S_6. Additionally, the peaks in the W 4f and O 1s spectra (Fig. 3c and d) shift to lower binding energies, indicating electron transfer from Li_2S_6 to W and O atoms.[40,41] Notably, two new pairs of peaks appear in the W 4f spectrum at 34.1/36.5 eV (corresponding to W^{5+}) and 33.3/35.8 eV (corresponding to W^{4+}), and the peak of O 1s at 531.7 eV was more intense than that before adsorption, both attributed to the formation of thiosulfate/polythionates.[36] Based on the adsorption test results and XPS analysis, it can be inferred that WO_3 interacts with soluble LiPS to form intermediate thiosulfate species, with LiPS donating electrons to WO_3, reducing W^{6+} to W^{5+}/W^{4+}.[36] Then, thiosulfate further interacts with higher-order LiPS, forming polythionate complexes and lower-order lithium polysulfides.[42,43] Thus, these thiosulfate species formed on the WO_3 surface function as a redox shuttle to catalyze LiPS conversion reactions, thereby suppressing the shuttle effect and

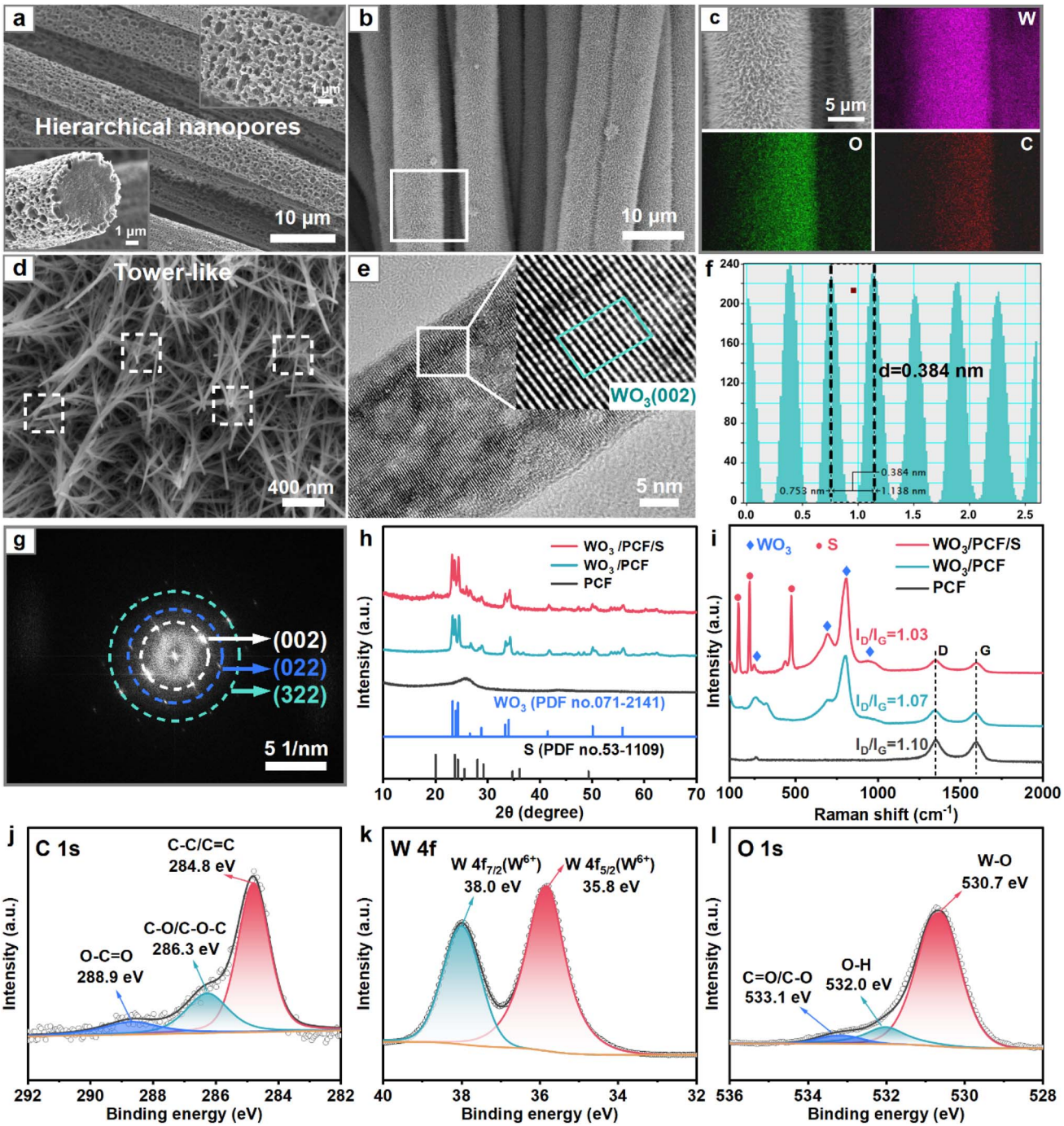

Fig. 2 (a and b) SEM images of PCF and WO_3/PCF, (c) EDS mappings of W, O, and C elements for the highlighted region in (b), (d) SEM images of PCF at high magnification, (e) TEM and HRTEM images of a single WO_3 nanowire, (f and g) interplanar spacing measurement and fast Fourier transform (FFT) pattern for the outlined region in (e), (h and i) XRD patterns and Raman spectra of PCF, WO_3/PCF and WO_3/PCF/S, and (j–l) high-resolution XPS spectra of C 1s, W 4f and O 1s for WO_3/PCF.

enhancing the conversion kinetics of LiPS, as illustrated in Fig. 1b.

The interaction between LiPS and WO_3 was further elucidated through density functional theory (DFT) calculations. The results reveal that S_8 molecules lie flat on the WO_3 surface with an adsorption energy of −3.18 eV, while Li_2S_x (x = 1–8) molecules were adsorbed on the WO_3 (002) surface *via* Li–O bonds with adsorption energies for Li_2S_8@WO_3, Li_2S_6@WO_3, Li_2S_4@WO_3, Li_2S_2@WO_3, and Li_2S@WO_3 being −4.64, −4.00, −4.24, −4.34, and −4.03 eV, respectively. During the adsorption process, long-chain Li_2S_8/Li_2S_6 undergo Li–S bond cleavage, while S–S bond lengths in short-chain Li_2S_2/Li_2S increase from 2.23/2.09 Å to 2.68/2.34 Å (Fig. S8† and 3e). This strong chemisorption of WO_3 towards LiPS, leading to the breaking of Li–S

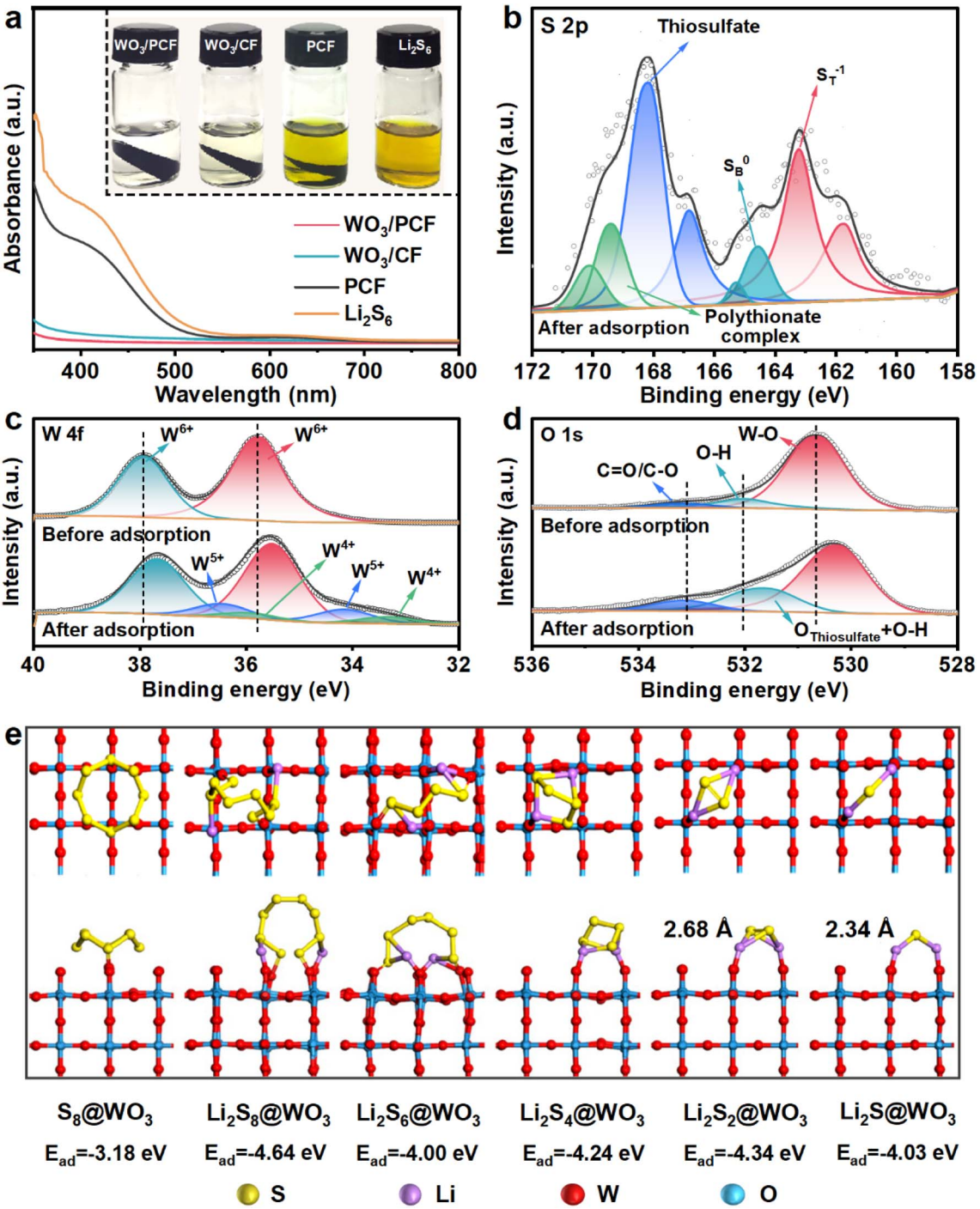

Fig. 3 (a) Optical images and UV-vis spectra of Li_2S_6 solution after absorption with WO_3/PCF, WO_3/CF, and PCF, (b–d) high-resolution XPS spectra of S 2p, W 4f and O 1s for WO_3/PCF before and after soaking in Li_2S_6 solution, and (e) optimized adsorption geometries and adsorption energies of S_8, Li_2S_8, Li_2S_6, Li_2S_4, Li_2S_2 and Li_2S on the WO_3 (002) surface.

bonds or stretching of S–S bonds, facilitates the conversion of LiPS ↔ Li_2S during charge/discharge cycles.[44]

To substantiate the high-efficiency sulfur conversion facilitated by WO_3/PCF, a series of electrochemical performances were evaluated on WO_3/PCF/S, WO_3/CF/S and PCF/S cathodes. Cyclic voltammetry (CV) was performed within a voltage range of 1.7–2.8 V (Fig. S9†). All CV curves exhibit two reduction peaks and one oxidation peak, corresponding to reduction of sulfur to soluble long-chain LiPS (Li_2S_x, $4 \leq x \leq 8$) and further reduction to solid-state short-chain Li_2S_2/Li_2S, and the reverse oxidation reactions.[45,46] Notably, the redox peaks of WO_3/PCF/S were sharper and more intense compared to other cathodes (Fig. 4a), indicating higher reaction activity and faster reaction kinetics. The reduction peaks shifted towards more positive potential

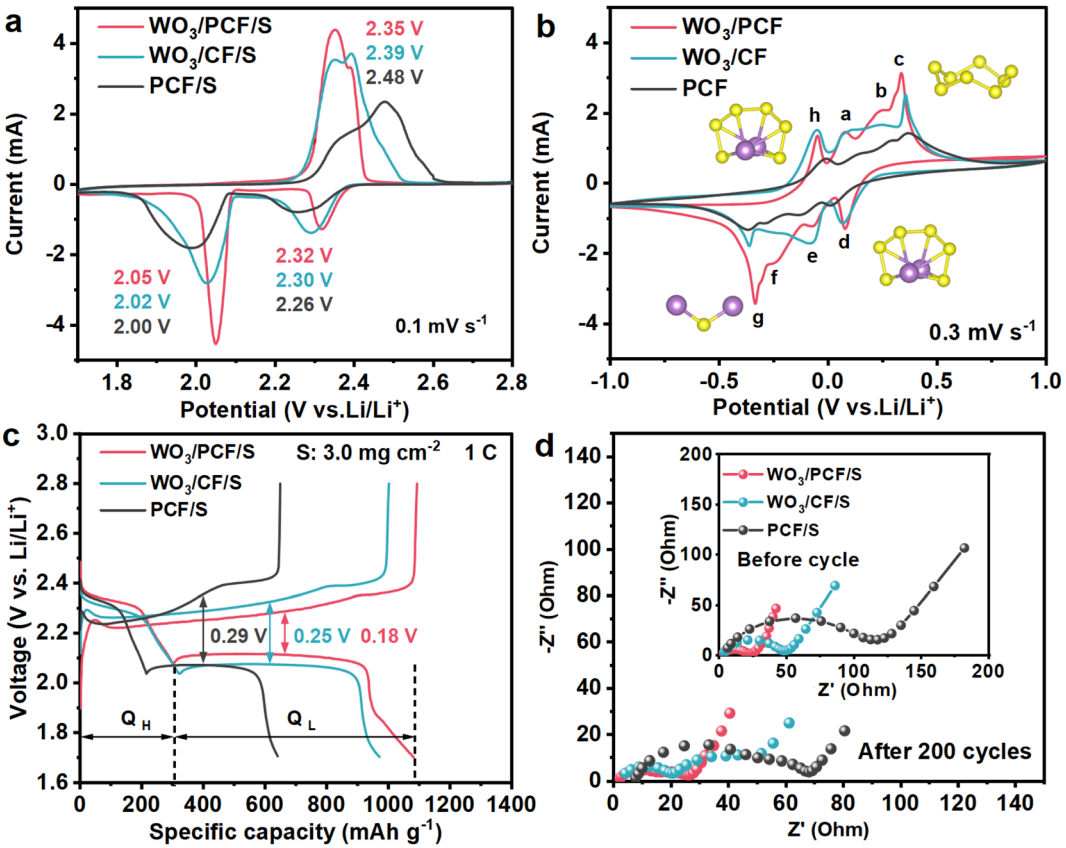

Fig. 4 (a and b) CV profiles of Li–S cells and symmetric cells based on WO_3/PCF, WO_3/CF and PCF electrodes, (c) charge–discharge voltage profiles of Li–S cells based on WO_3/PCF/S, WO_3/CF/S and PCF/S cathodes at 1 C for the first cycle, and (d) EIS spectra of WO_3/PCF/S, WO_3/CF/S and PCF/S in Li–S cells before and after 200 cycles at 1 C.

and the oxidation peak shifted towards more negative potential, suggesting reduced electrode polarization and enhanced redox reversibility. Similarly, in the CV curves of symmetrical cells (Fig. 4b), all electrodes display four pairs of redox peaks. Peaks a, b and c correspond to the stepwise oxidation of Li_2S_6 to S_8, while peaks d, e and f correspond to the stepwise reduction of S_8 to Li_2S_6 on the working electrode. At peak g, Li_2S_6 was reduced to Li_2S (or Li_2S_2), and at peak h, Li_2S (or Li_2S_2) was oxidized to Li_2S_6.[47,48] The WO_3/PCF/S electrode exhibited higher peak currents and closer redox potentials, with the peak currents for the four pairs of redox peaks occurring at 0.075/−0.070 V (peak a/peak e), 0.236/−0.226 V (peak b/peak f), 0.339/−0.334 V (peak c/peak g) and 0.049/−0.046 V (peak d/peak h), indicating superior redox kinetics and reversibility.

The galvanostatic charge–discharge (GCD) curves of WO_3/PCF/S, WO_3/CF/S, and PCF/S cathodes at 1 C for the 1st, 100th, 200th, 300th, 500th, and 1000th cycles show two discharge plateaus and one charging plateau, consistent with the CV analysis (Fig. S10†). The WO_3/PCF/S cathode demonstrates a higher overlap in its GCD curves, indicating superior cycling reversibility. The initial GCD curves (Fig. 4c) reveal that the WO_3/PCF/S cathode has a voltage hysteresis (ΔV) of only 0.18 V, significantly lower than those of WO_3/CF/S (0.25 V) and PCF/S (0.29 V), indicating minimal polarization and the fastest reaction kinetics. Additionally, Q_H is associated with the discharge plateau at 2.3 V, corresponding to the conversion of solid to soluble LiPS, while Q_L relates to the 2.0 V discharge plateau, indicating the conversion of soluble LiPS to solid Li_2S_2/Li_2S. The Q_H/Q_L ratio reflects the catalytic conversion efficiency in sulfur redox reactions.[49,50] The WO_3/PCF/S cathode has a Q_L/Q_H ratio of 2.59, much higher than those of WO_3/CF/S (2.01) and PCF/S (1.98), further demonstrating effective promotion of solid–liquid–solid sulfur conversion kinetics by WO_3/PCF. Electrochemical Impedance Spectroscopy (EIS) was conducted to assess the internal interface and charge transfer resistances (Fig. 4d, Table S1†). Prior to cycling, the EIS spectra show a single semicircle attributed to the charge transfer resistance semicircle (R_{ct}) of the cathode,[51,52] with an R_{ct} value of 19.25 Ω for WO_3/PCF/S, significantly lower than those for WO_3/CF/S (41.55 Ω) and PCF/S (98.35 Ω). After 200 cycles, all EIS spectra display two semicircles, with the emerging low-frequency semicircle indicating interfacial resistance (R_f), associated with the formation of an insulating Li_2S_2/Li_2S layer on the lithium anode surface.[40,53] The WO_3/PCF/S cathode exhibits an R_f of 10.71 Ω and an R_{ct} of 12.90 Ω, both significantly lower than those of WO_3/CF/S and PCF/S, indicating that the WO_3/PCF scaffold effectively mitigates the shuttle effect and reduces sulfur redox resistance during cycling.

WO_3/PCF/S also shows exceptional cycling and rate performance. At a sulfur loading of 3.0 mg cm^{-2}, it delivers an initial

discharge capacity of 1082 mA h·g^{-1} at 1 C, with a decay rate of only 0.039% over 1000 cycles, significantly outperforming WO_3/CF/S (991 mA h·g^{-1} and 0.065%) and PCF/S (641 mA h·g^{-1} and 0.070%) (Fig. 5a). At sulfur loadings of 2.2 mg cm^{-2} and 6.1 mg cm^{-2} (Fig. 5b), the WO_3/PCF/S cathode maintains decay rates of 0.028% and 0.043% at 0.5 C over 1000 cycles, respectively, demonstrating excellent cycling stability at high sulfur loadings. Additionally, at 0.2 C, 2 C, and 5 C, the WO_3/PCF/S cathode (3.0 mg cm^{-2} sulfur loading) shows capacity decay rates of 0.028%, 0.049%, and 0.058% over 1000 cycles, respectively, indicating stable cycling at high rates (Fig. 5c). Discharge capacities of WO_3/PCF/S at 0.2, 0.5, 1, 2, 3 and 5 C were 1356, 1035, 924, 841, 747 and 672 mA h·g^{-1}, respectively (Fig. 5d), superior to WO_3/CF/S and PCF/S cathodes, demonstrating the exceptional rate performance of the WO_3/PCF/S cathode. Self-discharge, assessed using the "cycle-rest" method, shows that at 0.5 C, the WO_3/PCF/S cathode retains 89.6% of its capacity after resting for 3 days, outperforming WO_3/CF/S (76.3%) and PCF/S (74.3%) (Fig. 5e). The suppression of the shuttle effect, quantified by measuring the shuttle current in potentiostatic mode,[54,55] shows that WO_3/PCF/S exhibits the lowest steady-state current (Fig. 5f), indicating effective suppression of the shuttle effect.

After cycling at 1 C for 200 cycles, the cathodes and separators from the disassembled cells were examined (insets of Fig. 6a–c). The separator from the cell with the WO_3/PCF/S cathode shows a very faint yellow color, indicating effective suppression of the shuttle effect *via* physical constraint and adsorption catalysis of LiPS by PCF and WO_3. Additionally, the cycled WO_3/PCF/S cathode maintains its tower-like cluster structure, unlike the collapsed structure of WO_3/CF/S and the porous structure of PCF/S. Furthermore, the undesired anode corrosion reaction between LiPS and the Li anode was significantly mitigated as well. After 200 cycles at 1 C, the Li anode that detached from the battery using the WO_3/PCF/S cathode exhibited a smooth and compact surface without visible holes or cracks (Fig. 6d). In contrast, the Li anodes cycled with WO_3/CF/S and PCF/S cathodes showed rough surfaces with notable porosity and fractures (Fig. 6e and f). Cross-sectional EDS mapping of F and S elements on the cycled Li anode reveals a well-defined interfacial layer. This layer is a dense, stable solid electrolyte interphase (SEI), formed from reactions involving polysulfides, the Li anode and electrolyte decomposition products (Fig. S11†), and primarily consists of inorganic compounds like Li_2O, LiF, Li_2SO_x, and Li_2S, along with certain organic molecules.[56,57] Moreover, the cycled Li anode in the WO_3/PCF/S

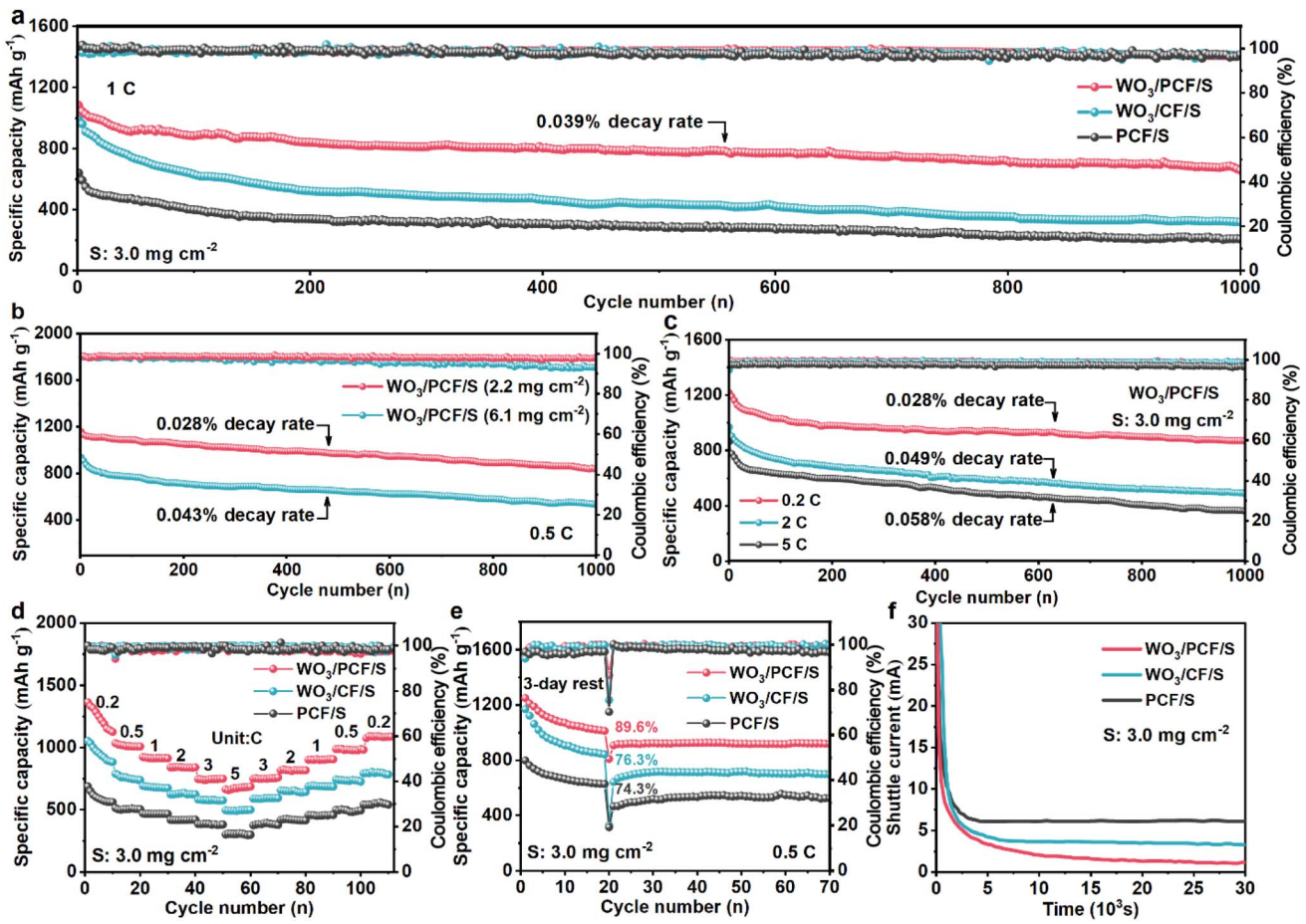

Fig. 5 Electrochemical performances of Li–S cells based on WO_3/PCF/S, WO_3/CF/S, and PCF/S cathodes: cycling performance (a) at a sulfur loading of 3.0 mg cm^{-2} at 1 C and (b and c) at different sulfur loadings and different rates, (d) rate performance, (e) self-discharge, and (f) shuttle current.

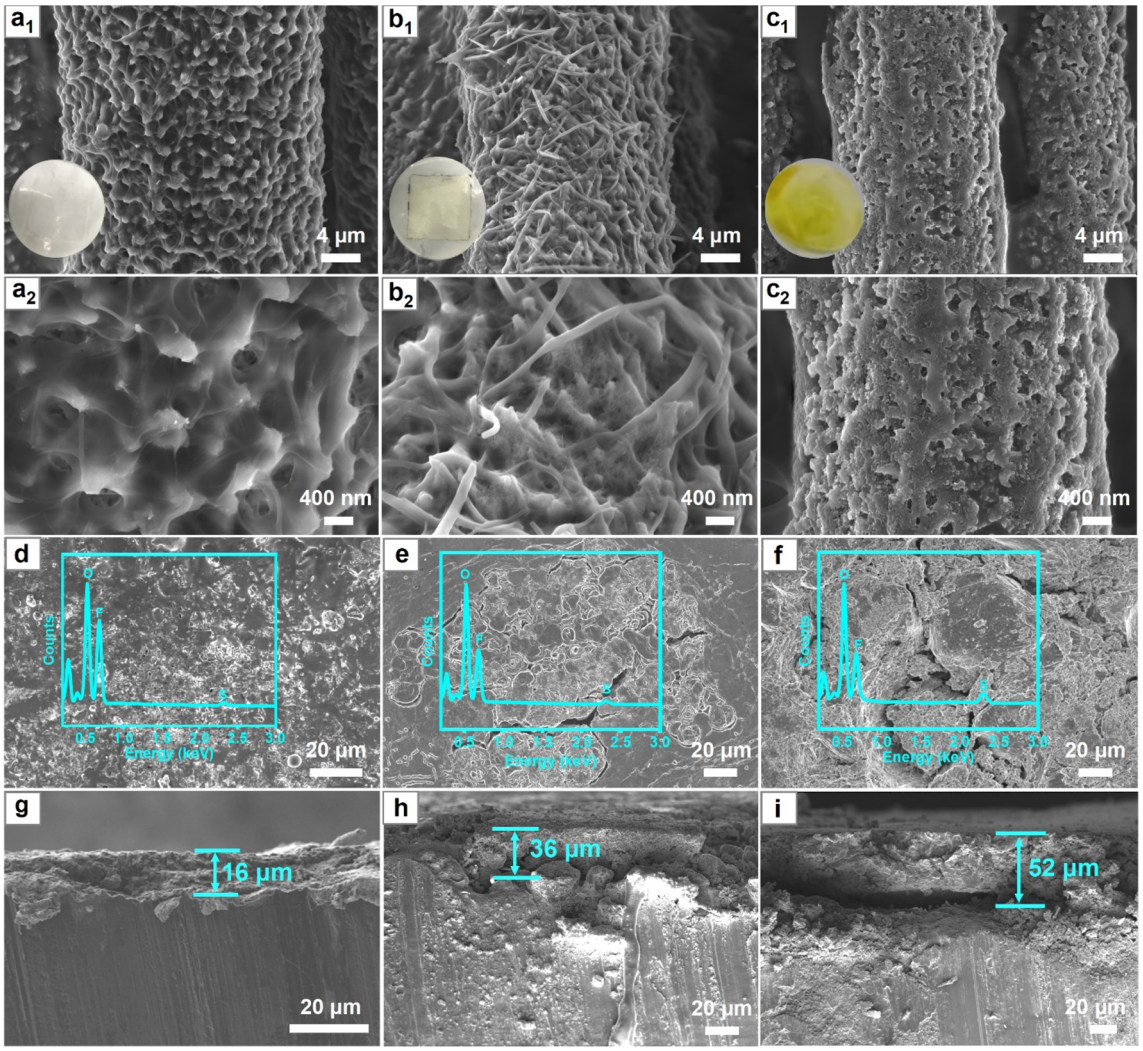

Fig. 6 (a–c) SEM and digital images of WO_3/PCF/S, WO_3/CF/S and PCF/S cathodes, separators and (d–i) Li metal anodes from the disassembled cells after 200 cycles at 1 C.

cell displayed a much thinner SEI layer (15 *vs.* 36/52 μm) (Fig. 6g–i), indicating significantly reduced anode corrosion. This underscores the dual-anchoring role of PCF towards WO_3 nanowire clusters and soluble polysulfides as well as the adsorption-catalysis role of WO_3 in the reversible conversion of sulfur species. As illustrated in Fig. 1c, for the PCF, the physical confinement of the surface porous carbon layer cannot prevent soluble polysulfides escaping from the PCF, while for WO_3/PCF, the WO_3 nanowire clusters on the PCF can effectively capture the escaping polysulfides and facilitate the conversion of LiPS ↔ Li_2S. Thus, such a flexible self-supporting WO_3/PCF/S cathode achieves high capacity, exceptional cycle stability and superior rate capability, surpassing those reported in recent studies, as shown in Table S2.†

Conclusions

In summary, we introduce a flexible, self-supporting composite scaffold featuring polar "tower-like" WO_3 nanowire clusters anchored on core–shell porous carbon fibers (WO_3/PCF) for sulfur accommodation. This distinctive architecture was fabricated using a combination of metal-assisted chemical etching followed by hydrothermal-annealing techniques. DFT theoretical calculations and extensive characterization reveal that the core of PCF acts as a robust electrode supporting scaffold, while the porous carbon shell forms a 3D interconnected conductive network that effectively accommodates active sulfur, suppresses polysulfide diffusion, and buffers electrode volume expansion. The WO_3 nanowire clusters capture LiPS escaping from the porous carbon network *via* polar–polar interactions and act as a redox mediator to accelerate sulfur conversion through reacting with LiPS to form thiosulfate/polythionate species, thereby mitigating the shuttle effect and enhancing redox kinetics. The combined advantages of self-supporting PCF and the dual functionality of WO_3 for LiPS capture and conversion contribute to the outstanding electrochemical performance of the WO_3/PCF/S cathode, including high capacity (1356 mA $h \cdot g^{-1}$ at 0.2 C), superior rate capability (672 mA $h \cdot g^{-1}$ at 5 C),

and exceptional cycling stability (an initial capacity of 1082 mA $h \cdot g^{-1}$ with an ultralow decay rate of 0.039% over 1000 cycles at 1 C), along with low self-discharge.

Data availability

The data supporting this article have been included as part of the ESI.† All experimental data are available from the corresponding author upon reasonable request.

Conflicts of interest

The authors declare that they have no conflict of interest.

Acknowledgements

This research was financially supported by the National Natural Science Foundation of China (52372187, 51972093, and U1910210), Higher Education Discipline Innovation Project "New Materials and Technology for Clean Energy" (No. B18018), Nature Science Research Project of Anhui Province (2008085ME129), and Key Research and Development Program of Anhui Province (2022h11020012).

References

1 W. H. Jin, X. Y. Zhang, M. Liu, Y. Zhao and P. Zhang, *Energy Storage Mater.*, 2024, **67**, 103223.
2 H. Raza, S. Y. Bai, J. Y. Cheng, S. Majumder, H. Zhu, Q. Liu, G. P. Zheng, X. F. Li and G. H. Chen, *Electrochem. Energy Rev.*, 2023, **6**, 29.
3 Y. Z. Huang, L. Lin, C. K. Zhang, L. Liu, Y. K. Li, Z. S. Qiao, J. Lin, Q. L. Wei, L. S. Wang, Q. S. Xie and D. L. Peng, *Adv. Sci.*, 2022, **9**, 2106004.
4 J. Tan, L. L. Ma, Y. Wang, P. S. Yi, C. M. Ye, Z. Fang, Z. H. Li, M. X. Ye and J. F. Shen, *Energy Environ. Mater.*, 2024, **7**, e12688.
5 W. Q. Yao, K. Liao, T. X. Lai, H. Sul and A. Manthiram, *Chem. Rev.*, 2024, **124**, 4935–5118.
6 J. T. Kim, X. G. Hao, C. H. Wang and X. L. Sun, *Matter*, 2023, **6**, 316–343.
7 M. Y. Wang, Z. C. Bai, T. Yang, C. H. Nie, X. Xu, Y. X. Wang, J. Yang, S. X. Dou and N. N. Wang, *Adv. Energy Mater.*, 2022, **12**, 2201585.
8 C. Yuan, X. F. Yang, P. Zeng, J. Mao, K. H. Dai, L. Zhang and X. L. Sun, *Nano Energy*, 2021, **84**, 105928.
9 M. Waqas, Y. H. Niu, M. J. Tang, Y. S. Pang, S. Ali, Y. F. Dong, W. Q. Lv and W. D. He, *Energy Storage Mater.*, 2024, **72**, 103682.
10 X. X. Zhu, L. G. Wang, Z. Y. Bai, J. Lu and T. P. Wu, *Nano-Micro Lett.*, 2023, **15**, 75.
11 B. B. Gicha, L. T. Tufa, N. Nwaji, X. J. Hu and J. Lee, *Nano-Micro Lett.*, 2024, **16**, 172.
12 S. Maiti, M. T. Curnan, K. Kim, K. Maiti and J. K. Kim, *Adv. Energy Mater.*, 2024, 2401911.
13 Y. Z. Song, L. W. Zou, C. H. Wei, Y. Zhou and Y. Hu, *Carbon Energy*, 2023, **5**, e286.
14 J. Wu, T. Ye, Y. C. Wang, P. Y. Yang, Q. C. Wang, W. Y. Kuang, X. L. Chen, G. H. Duan, L. M. Yu, Z. Q. Jin, J. Q. Qin and Y. P. Lei, *ACS Nano*, 2022, **16**, 15734–15759.
15 S. G. Deng, T. Z. Guo, J. Heier and C. F. Zhang, *Adv. Sci.*, 2023, **10**, 2204930.
16 H. C. Li, X. Y. Wang, H. W. Ma, D. Y. Guo, L. H. Wu, H. L. Jin and X. A, *ChemElectroChem*, 2024, **11**, e202300696.
17 G. Y. Zhu, Q. Z. Wu, X. H. Zhang, Y. W. Bao, X. Zhang, Z. Y. Shi, Y. Z. Zhang and L. B. Ma, *Nano Res.*, 2024, **17**, 2574–2591.
18 J. L. Cheong, C. Hu, W. W. Liu, M. F. Ng, M. B. Sullivan and J. Y. Ying, *Nano Energy*, 2022, **102**, 107659.
19 P. Wang, B. J. Xi, M. Huang, W. H. Chen, J. K. Feng and S. L. Xiong, *Adv. Energy Mater.*, 2021, **11**, 2002893.
20 Y. Yang, B. W. Sun, Z. Q. Sun, J. J. Xue, J. H. He, Z. H. Wang, K. N. Sun, Z. X. Sun, H. K. Liu and S. X. Dou, *Coordin. Chem. Rev.*, 2024, **510**, 215836.
21 Y. Hu, W. Chen, T. Y. Lei, Y. Jiao, J. W. Huang, A. J. Hu, C. H. Gong, C. Y. Yan, X. F. Wang and J. Xiong, *Adv. Energy Mater.*, 2020, **10**, 2000082.
22 Q. H. Q. Xiao, J. L. Yang, X. D. Wang, Y. R. Deng, P. Han, N. Yuan, L. Zhang, M. Feng, C. A. Wang and R. P. Liu, *Carbon Energy*, 2021, **3**, 271–302.
23 Z. Y. Geng, T. Meng, F. Ma, W. C. Qin, X. H. Wang, H. F. Zhang and G. Guan, *Adv. Funct. Mater.*, 2024, **34**, 2309345.
24 G. Kresse and J. Furthmüller, *Comp. Mater. Sci.*, 1996, **6**, 15–50.
25 G. Kresse and J. Furthmüller, *Phys. Rev. B: Condens. Matter Mater. Phys.*, 1996, **54**, 11169–11186.
26 J. P. Perdew, K. Burke and M. Ernzerhof, *Phys. Rev. Lett.*, 1996, **77**, 3865–3868.
27 H. J. Monkhorst and J. D. Pack, *Phys. Rev. B: Condens. Matter Mater. Phys.*, 1976, **13**, 5188–5192.
28 L. B. Ni, S. Q. Duan, H. Y. Zhang, J. Gu, G. J. Zhao, Z. X. Lv, G. Yang, Z. Y. Ma, Y. Liu, Y. S. Fu, Z. Wu, J. Xie, M. Chen and G. W. Diao, *Carbon*, 2021, **182**, 335–347.
29 C. Y. Zhang, G. W. Sun, Y. F. Bai, Z. Dai, Y. R. Zhao, X. P. Gao, G. Z. Sun, X. B. Pan, X. J. Pan and J. Y. Zhou, *J. Mater. Chem. A*, 2020, **8**, 18358–18366.
30 B. Zhang, C. Luo, Y. Q. Deng, Z. J. Huang, G. M. Zhou, W. Lv, Y. B. He, Y. Wan, F. Y. Kang and Q. H. Yang, *Adv. Energy Mater.*, 2020, **10**, 2000091.
31 S. Choi, D. H. Seo, M. R. Kaiser, C. Zhang, V. D. L. Timothy, Z. J. Han, A. Bendavid, X. Guo, S. Yick, A. T. Murdock, D. Su, B. R. Lee, A. Du, S. X. Dou and G. X. Wang, *J. Mater. Chem. A*, 2019, **7**, 4596–4603.
32 C. Nims, B. Cron, M. Wetherington, J. Macalady and J. Cosmidis, *Sci. Rep.*, 2019, **9**, 7971.
33 S. G. Deng, X. T. Shi, Y. Zhao, C. Wang, J. H. Wu and X. Y. Yao, *Chem. Eng. J.*, 2022, **433**, 133683.
34 G. C. Ruan, Y. R. Shen, J. Yao, Y. W. Huang, S. Y. Yang, S. J. Hu, H. Q. Wang, Y. P. Fang and X. Cai, *J. Power Sources*, 2023, **566**, 232922.
35 X. Y. Yang, H. L. Zu, L. Q Luo, H. W. Zhang, J. Y. Li, X. B. Yi, H. Liu, F. Y. Wang and J. J. Song, *J. Alloy. Compd.*, 2020, **833**, 154969.

36 S. K. Lee, H. Kim, S. Bang, S. T. Myung and Y. K. Sun, *Molecules*, 2021, **26**, 377.
37 Y. Kong, X. Ao, X. Huang, J. L. Bai, S. Q. Zhao, J. Y. Zhang and B. B. Tian, *Adv. Sci.*, 2022, **9**, 2105538.
38 J. Q. Liu, K. H. Li, Q. Zhang, X. F. Zhang, X. Liang, J. Yan, H. H. Tan, Y. Yu and Y. C. Wu, *ACS Appl. Mater. Interfaces*, 2021, **13**, 45547–45557.
39 Y. B. Wang, D. Y. Zhang, J. H. Han, Y. Yang, Y. Guo, Z. X. Bai, J. B. Cheng, P. L. K. Chu, H. Pang and Y. S. Luo, *Chem. Eng. J.*, 2022, **433**, 133629.
40 F. Ma, Z. Chen, K. Srinivas, Z. H. Zhang, Y. Wu, D. W. Liu, H. S. Yu, Y. Wang, X. S. Li, M. Q. Zhu, Q. Wu and Y. F. Chen, *J. Energy Chem.*, 2024, **88**, 260–271.
41 J. H. Li, Z. Y. Wang, K. X. Shi, Y. J. Wu, W. Z. Huang, Y. G. Min, Q. B. Liu and Z. X. Liang, *Adv. Energy Mater.*, 2024, **14**, 2303546.
42 X. Liang, C. Hart, Q. Pang, A. Garsuch, T. Weiss and L. F. Nazar, *Nat. Commun.*, 2015, **6**, 5682.
43 H. Chen, W. D. Dong, F. J. Xia, Y. J. Zhang, M. Yan, J. P. Song, W. Zou, Y. Liu, Z. Y. Hu, J. Liu, Y. Li, H. E. Wang, L. H. Chen and B. L. Su, *Chem. Eng. J.*, 2020, **381**, 122746.
44 M. X. Wang, L. S. Fan, X. Sun, B. Guan, B. Jiang, X. Wu, D. Tian, K. N. Sun, Y. Qiu, X. J. Yin, Y. Zhang and N. Q. Zhang, *ACS Energy Lett.*, 2020, **5**, 3041–3050.
45 T. T. Sun, C. Huang, H. B. Shu, L. P. Luo, Q. Q. Liang, M. F. Chen, J. C. Su and X. Y. Wang, *ACS Appl. Mater. Interfaces*, 2020, **12**, 57975–57986.
46 Y. Y. Kong, L. Wang, M. Mamoor, B. Wang, G. M. Qu, Z. X. Jing, Y. P. Pang, F. B. Wang, X. F. Yang, D. D. Wang and L. Q. Xu, *Adv. Mater.*, 2023, **36**, 2310143.
47 M. D. Zhang, J. W. Mu, Y. N. Li, Y. Y. Pan, Z. L. Dong, B. Chen, S. W. Guo, W. H. Yuan, H. W. Fang, H. Hu and M. B. Wu, *J. Energy Chem.*, 2023, **78**, 105–114.
48 T. Liu, S. N. Fu, S. S. X, J. Li, H. T. Cui, Y. Y. Liu, K. H. Liu, H. Y. Wei and M. R. Wang, *Appl. Surf. Sci.*, 2024, **655**, 159617.
49 Q. W. Ran, J. T. Liu, L. Li, Q. Hu, H. Y. Zhao, S. Komarneni and X. Q. Liu, *Adv. Funct. Mater.*, 2024, **34**, 2402872.
50 B. Wang, J. Y. Tang, S. Y. Jia, Z. Q. Xing, S. W. Chen, Y. Deng, X. K. Meng and S. C. Tang, *Adv. Funct. Mater.*, 2024, **34**, 2315836.
51 K. L. Liu, X. D. Zhang, F. J. Miao, Z. Wang, S. J. Zhang, Y. S. Zhang, P. Zhang and G. S. Shao, *Small*, 2021, **17**, 2100065.
52 G. Z. Zhang, H. M. Deng, R. M. Tao, B. Q. Xiao, T. Y. Hou, S. Yue, N. Shida, Q. Cheng, W. X. Zhang and J. Y. Liang, *Mater. Lett.*, 2020, **262**, 127194.
53 M. Luo, Y. Bai, R. Sun, M. X. Qu, M. Y. Wang, Z. F. Yang, Z. H. Wang, W. Sun and K. N. Sun, *J. Energy Chem.*, 2022, **73**, 407–415.
54 P. Cheng, L. L. Shi, W. Q. Li, X. R. Fang, D. L. Chao, Y. G. Zhao, P. Cao, D. Q. Liu and D. Y. He, *Small*, 2023, **19**, 2206083.
55 Z. F. Li, M. Zhang, Y. Liu, Y. Cao, Q. H. Zeng, Q. J. Mao, Z. H. Lu, Y. C. Jiang, A. Q. Chen, J. Z. Guan, H. H. Wang, L. Chen, R. Z. Li, Y. J. Zhou, J. C. Wang, X. F. Liu, X. Y. Liu and L. Y. Zhang, *Adv. Funct. Mater.*, 2024, 2412579.
56 H. J. Yang, Y. Qiao, Z. Chang, P. He and H. S. Zhou, *Angew. Chem., Int. Ed.*, 2021, **60**, 17726–17734.
57 L. S. Wu, J. P. Hu, S. J. Chen, X. R. Yang, L. Liu, J. S. Foord, P. Pobedinskas, K. Haenen, H. J. Hou and J. K. Yang, *Electrochim. Acta*, 2023, **466**, 142973.